A two-stage approach for quantitative damage imaging in metallic plates using Lamb waves

Ching-Tai Ng[*]

School of Civil, Environmental & Mining Engineering, University of Adelaide
Adelaide, SA 5005, Australia

Abstract. This paper proposes a two-stage imaging approach for quantitative inspection of damages in metallic plates using the fundamental anti-symmetric mode of (A_0) Lamb wave. The proposed approach employs a number of transducers to transmit and receive A_0 Lamb wave pulses, and hence, to sequentially scan the plate structures before and after the presence of damage. The approach is applied to image the corrosion damages, which are simplified as a reduction of plate thickness in this study. In stage-one of the proposed approach a damage location image is reconstructed by analyzing the cross-correlation of the wavelet coefficient calculated from the excitation pulse and scattered wave signals for each transducer pairs to determine the damage location. In stage-two the Lamb wave diffraction tomography is then used to reconstruct a thickness reduction image for evaluating the size and depth of the damage. Finite element simulations are carried out to provide a comprehensive verification of the proposed imaging approach. A number of numerical case studies considering a circular transducer network with eight transducers are used to identify the damages with different locations, sizes and thicknesses. The results show that the proposed methodology is able to accurately identify the damage locations with inaccuracy of the order of few millimeters of a circular inspection area of 100 mm^2 and provide a reasonable estimation of the size and depth of the damages.

Keywords: diffraction tomography; lamb waves; laminar damage; scattering; damage identification

1. Introduction

Early detection of damage in structures is crucial to avoid costly repairs and essential to prevent catastrophic failure. Different inspection methods have been developed to ensure the safety of civil, mechanical and aerospace structures (Carden and Fanning 2004, Farrar and Worden 2007, Lam *et al*. 2008, Ng *et al*. 2009a), all of which are prone to deterioration over time. Of all the causes of deterioration, corrosion is the most ubiquitous. A study by Virrmani in 2002 showed that the estimated cost of the corrosion ranges from 1-5% of most countries' gross national product (2002). Therefore, detection and sizing of corrosion in metallic structures using new technologies is of growing interest in a wide range of engineering industries. Conventional ultrasonic and eddy current methods (Achenbach 2000) have been commonly employed in industry for detecting and

---

∗Corresponding author, Ph.D., E-mail: alex.ng@adelaide.edu.au

sizing the corrosion. However, one major limitation of these techniques is that they are only able to inspect the area covered by the probe. This makes the inspection process time consuming when investigating large structural areas, and cannot be used for inspecting inaccessible areas. Therefore, it is important to develop a reliable technique for rapid, accurate and long range inspection of damage.

In the last decade, Lamb waves have received considerable attention (Alleyen *et al*. 2001, Rose 2002) because they are highly sensitive to small and different types of damages in structures. Moreover, Lamb waves are able to propagate a long distance, and can be used to inspect a large area of a structure. Apart from the essential requirement that inspection systems must be reliable, two highly desirable features are a capacity for graphic representation and the ability to evaluate damage quantitatively. Quantitative imaging of damage provides information about not only the location, but also the size and depth of the damage. A number of quantitative damage imaging techniques using Lamb waves have been proposed in the literature, such as a pre-stack reverse-time migration technique (Lin and Yuan 2001), tomography (Jansen and Hutchins 1990) and diffraction tomography (Malyarenko and Hinders 2001). The method proposed in this paper is a two-stage approach, which is an extension of Lamb wave diffraction tomography, using Lamb waves for the quantitative imaging of plate thickness reduction.

1.1 Background of the proposed method

Within the context of Lamb waves, the fundamental idea of tomography is to using Lamb wave propagation characteristics to reconstruct a spatial distribution of the material properties of an unknown object from projection data. The first investigation of the use of tomography to reconstruct an image of damage based on the time-of-flight information from Lamb waves was undertaken by Jansen and Hutchins (1990). Their study assumed the Lamb wave propagation was in the form of straight rays. A decade later, a research team led by Hinders carried out a number of studies in Lamb wave tomography. Malyarenko and Hinders (2000), Leonard *et al*. (2002) studied a number of time-of-flight tomography algorithms using Lamb waves and provided an extensive bibliography of literature in this research area. Leonard and Hinders (2005) subsequently demonstrated that time-of-flight Lamb wave tomography could be used for inspecting curved panels. Recently, Belanger and Cawley (2009) investigated the feasibility of using low frequency Lamb waves in time-of-flight tomography. They concluded that the straight-ray assumption was not valid for Lamb wave scattering at damage.

Malyarenko and Hinders (2001) proposed including diffraction in the time-of-flight Lamb wave tomography. They compared the performance of time-of-flight tomography with the straight-ray assumption, and the incorporation of the diffraction effect in the reconstruction. The study showed that Lamb wave diffraction tomography could further improve image quality and resolution. Belanger *et al*. (2010) proposed a time-of-flight diffraction tomography within the Born approximation using low frequency Lamb waves. Their study employed a transducer network with 64 transducers to evaluate reduction in plate thickness. The results showed that the damage location, size and depth could be accurately determined. Recently Huthwaite *et al*. (2013) introduced a hybrid algorithm for robust breast ultrasound tomography to the field of Lamb wave tomography. They demonstrated that the hybrid algorithm could further improve the resolution of the reconstructed image.

Wang and Rose (2003) proposed a Lamb wave diffraction tomography framework based on Mindlin plate theory for imaging inhomogeneities, such as change in Young's modulus, shear

modulus, density or plate thickness. The reconstruction was based on the Born approximation of scattered waves, and a direct Fourier inversion approach was used to reconstruct the damage image. Rohde *et al.* (2008) examined the performance of the Mindlin plate theory-based Lamb wave diffraction tomography with a fixed parallel transducer network using numerical simulation data, but found that a large number of measurement locations were required to obtain sufficient scattered wave data for unbiased reconstruction. A year later, using the far-field Born approximation, Rohde *et al.* (2009) demonstrated that reconstruction of the damage image could be achieved by using eight transducers only. Rose and Wang (2010) proposed a computationally efficient, filtered back-propagation algorithm to further improve Mindlin plate theory-based Lamb wave diffraction tomography. Wang and Rose (2013) carried out study of the minimum sensor density in the context of the diffraction tomography. They showed that the number of sensors required for in-situ imaging of damages in plates using diffraction tomography approach could be reduced through understanding of the mathematical structure, properties of the multistatic data matrix and the reconstruction algorithm. Recently Chan *et al.* (2014) proposed a generic diffraction tomography framework for imaging damage in plates. The capability of the proposed method was demonstrated using numerical simulations and experimental data.

1.2 The proposed method

The current study focused on further development of the Mindlin plate theory-based Lamb wave diffraction tomography. Although the far-field Born approximation approach could substantially reduce the number of measurement locations for scattered waves, this approach essentially assumes the damage is at the center of the transducer network. This limits the capacity of the method in practical applications. The study reported in this paper therefore had two main objectives. The first was to overcome the unintentional centering of the damage by introducing a two-stage approach. In stage-one, the location of the damage is determined. In stage-two, the same set of the scattered wave data is modified based on the identified damage location and used to reconstruct the damage image following Lamb wave diffraction tomography. The second objective was to provide a comprehensive numerical verification of Lamb wave diffraction tomography in order to assess the quality of the reconstructed image for different conditions of damages. It should be noted that the framework of the Lamb wave diffraction tomography was developed based on the assumption of a single wave mode. The current study also investigated the performance of Lamb wave diffraction tomography when wave scattering was affected by mode conversion.

The paper is organized as follows. Section 2 introduces the two-stage approach for quantitative imaging of damage in plate structures. Section 2.1 describes the first stage of the proposed methodology. It is a framework for reconstructing an image to determine the damage location by analyzing the cross-correlation between the excitation pulse and scattered waves. The second stage of the proposed methodology is then discussed in Section 2.2. In stage-two, the identified damage location from stage-one is incorporated into the Mindlin plate theory-based Lamb wave diffraction tomography in order to achieve a more practical quantitative imaging of the damage. Section 3 presents a comprehensive numerical verification of the proposed method using three-dimensional (3D) explicit finite element (FE) simulations. A number of numerical case studies, which target different damage conditions, are used to assess the performance of the proposed two-stage imaging approach. Finally, conclusions are presented in Section 4.
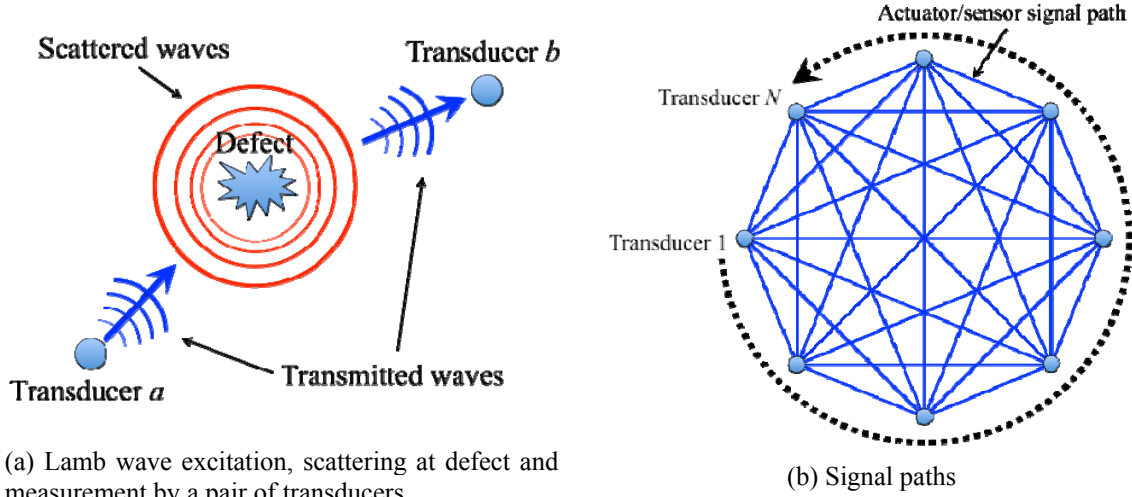
(a) Lamb wave excitation, scattering at defect and
measurement by a pair of transducers

(b) Signal paths

Fig. 1 Schematic diagram of the imaging algorithm

2. Two-stage approach for quantitative imaging of laminar damage

The proposed method is a two-stage approach that provides quantitative imaging of laminar damage in plate-like structures using the fundamental asymmetric mode (A_0) of Lamb wave. It utilizes a distributed network of N transducers, in which each transducer acts as both actuator and sensor to excite and measure the Lamb wave signals. In stage-one an image indicating the location of the damage is reconstructed by analyzing the cross-correlation of the damage information extracted from the incident pulse and scattered wave signals. Using the same set of data, and based on the identified damage location, an image indicating the size and depth of the damage can then be reconstructed by Lamb wave diffraction tomography in stage-two.

Both imaging algorithms in stages-one and -two rely on the same sequential scan process, in which one of the transducers is used to excite the A_0 Lamb wave while the rest of the transducers, i.e., N-1 transducers, are used for measuring the impinging waves. Fig. 1(a) shows a schematic diagram of two transducers a and b, which is a pair of the transducers in the distributed transducer network, for illustrating the scan process. As an example, transducer a is used to actuate the Lamb wave while transducer b is used for sensing. Wave scattering occurs when the incident wave interacts with the damage, as shown in Fig. 1(a). Considering the process shown in Fig. 1(a) as an actuator/sensor signal path, a distributed network of N transducers would result in total of $N(N$-1) actuator/sensor signal paths as shown in Fig. 1(b). The measured Lamb wave signals by transducer b contain both incident wave and scattered wave signals, but the damage information exists in the scattered wave signal only. Hence, a baseline subtraction process (Veidt and Ng 2011) is required to extract the scattered signal u_{ab}^S as

$$u_{ab}^S = u_{ab}^D - u_{ab}^{UD} \tag{1}$$

where u_{ab}^D and u_{ab}^{UD} are the measured signals from damaged and intact structures, respectively. The extracted scattered wave signals are then processed by the imaging algorithm in stage-two of the proposed method for quantitative identification of the damage. Sections 2.1 and 2.2 describe

the details of the imaging algorithm based on the cross-correlation analysis and Lamb wave diffraction tomography for determining the damage location and quantitatively identifying the damage.

2.1 Stage-one: Identification of damage location based on cross-correlation analysis

Using the scattered wave signals obtained from the sequential scan and baseline subtraction process, an image indicating the damage location can be generated by analyzing the cross-correlation of the incident pulse and scattered wave signals. The damage location can be identified by discretizing the inspection area into a set of image pixels located at (x,y). Using transducers a and b in Fig. 1(a) as an example, the inspection area can be discretized by image pixels as shown in Fig. 2. The image pixel at (x,y) contributed by the transducers a and b is defined as (Wang *et al.* 2004, Ng and Veidt 2009)

$$I_{ab}(x,y) = C_{ab}\left(T_{ab}(x,y)\right) \tag{2}$$

where T_{ab} is the arrival time of the scattered wave corresponding to the wave travelling from the transducer a at (x_a, y_a) to the image pixel I_{ab} at (x,y) and then from the image pixel to the transducer b at (x_b,y_b) and is defined as

$$T_{ab}(x,y) = \frac{\sqrt{(y_b - y)^2 + (x_b - x)^2} + \sqrt{(y - y_a)^2 + (x - x_a)^2}}{c_g} \tag{3}$$

Since the structure is designed and the transducer network is installed before carrying out the damage inspection, the location of the transducers, (x_a,y_a) and (x_b,y_b), is known in advance. c_g is the group velocity of the A_0 Lamb wave that can be determined theoretically or measured experimentally. C_{ab} is the cross-correlation between the incident pulse generated by transducer a
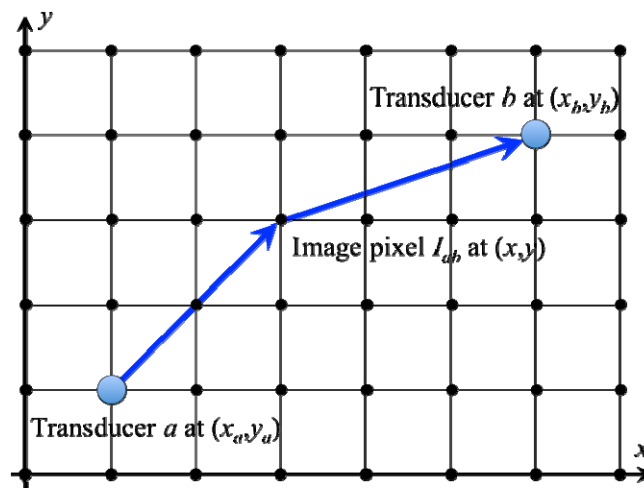

Fig. 2 Discretization of inspection area by image pixels and characteristic parameters for the proposed damage imaging algorithm based on cross-correlation analysis

and the scattered wave signal measured by transducer *b* which determines a time shift describing the location of the scattering source. For the proposed method, the continuous Gabor wavelet transform is employed to enhance the accuracy of the cross-correlation analysis. Hence, the cross-correlation C_{ab} is defined as (Ng *et al*. 2009b)

$$C_{ab}(t) = \int_0^T \left| WT_{ab}^S(\tau) \right| \left| WT^F(\tau + t) \right| d\tau \tag{4}$$

where *T* is the duration of the measured signals. WT_{ab}^S is the wavelet coefficient of the scattering signal at excitation frequency, in which transducers *a* and *b* act as actuator and sensor, respectively. WT^F is the wavelet coefficient of the excitation pulse at the excitation frequency. These wavelet coefficients can be calculated by continuous Gabor wavelet transform (Kishimoto *et al*. 1995, Ng *et al*. 2009b) as

$$WT(p,q) = \int_{-\infty}^{\infty} u(t) \frac{1}{\sqrt{q}} \bar{\psi}\left(\frac{t-p}{q}\right) dt \tag{5}$$

where $u(t)$ is an arbitrary time series representing the scattering signal $u_{ab}^{(s)}$ and excitation pulse in this study. *p* and *q* are the translation parameter and scaling parameter controlling the shift of the wavelet in time and wavelet frequency bandwidth. $\bar{\psi}$ is the complex conjugate of the mother wavelet ψ and is defined as

$$\psi_{p,q}(t) = \frac{1}{\sqrt{q}} \psi\left(\frac{t-p}{q}\right) \tag{6}$$

As the Gabor function's well-defined frequency characteristics are useful for extracting a particular harmonic component of dispersive waves, it is employed as the mother wavelet in this study. The Gabor function is defined as

$$\psi_G(t) = \frac{1}{\sqrt[4]{\pi}} \sqrt{\frac{\omega_0}{\mu}} \exp\left[-\frac{(\omega_0/\mu)^2}{2} t^2 + i\omega_0 t \right] \tag{7}$$

where ω_0 and μ are positive constants and are usually chosen as 2π and $\pi\sqrt{2/\ln 2} \approx 5.336$ (Kishimoto *et al*. 1995), respectively.

For each actuator and sensor signal path, an image indicating the possible locations of the damage can be reconstructed using Eq. (2). The actuator and sensor signal path image is an ellipse formed by image pixels with identical relative intensity with two foci at the locations of transducers *a* and *b*. For the distributed network of *N* transducers as shown in Fig. 1(b), the image indicating the location of the damage can be reconstructed by superimposing the power flux of *N*(*N*-1) actuator and sensor signal path images as (Wang *et al*. 2004, Ng and Veidt 2009)

$$I(x,y) = \sum_{a=1}^{N} \sum_{b=1, b \neq a}^{N} \eta_{ab} I_{ab}^2 \tag{8}$$

where η_{ab} are the weighting factors to account for varying sensitivities of individual transducers and are equal to unity for uniform aperture weighting.

2.2 Stage-two: Quantitative imaging of defect based on Lamb wave diffraction tomography

After the defect location is determined in stage-one, the same set of scattered wave signals can then be employed for quantitative imaging of the damage using Lamb wave diffraction tomography (Wang and Rose 2003, Rohde *et al*. 2008, Rose and Wang 2010). This damage imaging reconstruction framework was developed based on Mindlin plate theory to represent Lamb wave scattering by inhomogeneities with the consideration of the wave field diffraction. The following sub-sections describe the detail of representing the damage by perturbation functions, Born approximation of the scattered waves and image reconstruction by direct Fourier inversion approach.

2.1.1 Representation of defect by perturbation functions
Within the framework of Mindlin plate theory, the equations of motion are given by (Graff 1991)

$$\frac{\partial M_{xx}}{\partial x} + \frac{\partial M_{yx}}{\partial y} - Q_x + \rho I \frac{\partial^2 \Omega_x}{\partial t^2} = m_x$$

$$\frac{\partial M_{xy}}{\partial x} + \frac{\partial M_{yy}}{\partial y} - Q_y + \rho I \frac{\partial^2 \Omega_y}{\partial t^2} = m_y \tag{9}$$

$$\frac{\partial Q_x}{\partial x} + \frac{\partial Q_y}{\partial y} - \rho h \frac{\partial^2 w}{\partial t^2} = f$$

where M_{xx}, M_{yy}, M_{xy}, and M_{yx} are the bending moments, noting that $M_{xy}=M_{yx}$. Q_x and Q_y are the shear forces. Ω_x, Ω_y and w are in-plane rotations and plate-normal defection, respectively. ρ is the density of the material. $I=h^3/12$ is the moment of inertia and h is the thickness of the plate. m_x, m_y and f are the distributed bending moments and lateral pressure, respectively. The bending moments and the shear force can be related to rotations and deflections by

$$M_{xx} = -D\left(\frac{\partial \Omega_x}{\partial x} + v\frac{\partial \Omega_y}{\partial y}\right)$$

$$M_{yy} = -D\left(\frac{\partial \Omega_y}{\partial y} + v\frac{\partial \Omega_x}{\partial x}\right)$$

$$M_{xy} = -\frac{(1-v)}{2}D\left(\frac{\partial \Omega_y}{\partial x} + \frac{\partial \Omega_x}{\partial y}\right) \tag{10}$$

$$Q_x = \kappa^2 Gh\left(\frac{\partial w}{\partial x} - \Omega_x\right)$$

$$Q_y = \kappa^2 Gh\left(\frac{\partial w}{\partial y} - \Omega_y\right)$$

where $D=Eh^3/[12(1-v^2)]$ is the plate bending stiffness. E and v are the Young's modulus and Poisson's ratio. G is the shear modulus and $K = \pi/\sqrt{12}$ is the shear correction factor for accurate representation of the low frequency behavior (Graff 1991). In the current study a damage region Σ is treated as an inhomogeneity with reduced flexural stiffness. The fundamental plate-theory variables in the damage region Σ are represented by local perturbations as (Rose and Wang 2010)

$$D^\Sigma = \left[1 + s_1(\mathbf{x})\right]D$$

$$\left(\kappa^2 Gh\right)^\Sigma = \left[1 + s_2(\mathbf{x})\right]\kappa^2 Gh$$

$$\left(\rho I\right)^\Sigma = \left[1 + s_3(\mathbf{x})\right]\rho I \tag{11}$$

$$\left(\rho h\right)^\Sigma = \left[1 + s_4(\mathbf{x})\right]\rho h$$

where the fundamental plate-theory variables with superscript Σ represent the plate properties within the damage region Σ. $\mathbf{x}=(x,y)$ is an arbitrary location. $s_i(\mathbf{x})$ for i=1,2,3,4 are the perturbation functions which are non-zero within the damage region $\mathbf{x} \in \Sigma$. The fundamental plate-theory variables within the damage region in Eq. (11) have smaller values than those outside the damage region. The quantitative imaging of damage is achieved by reconstructing the perturbation functions $s_i(\mathbf{x})$ from the same set of scattered signals obtained in Section 2.1.

2.1.2 Born approximation of scattered waves

It can be assumed that the deflection potential of the incident wave at the excitation frequency ω can be represented as (Wang *et al*. 2004)

$$\hat{u}^I(\mathbf{x},\omega) = e^{i\mathbf{k}_1^I \cdot \mathbf{x}} \tag{12}$$

where $\mathbf{k}_1^I = k_1[\cos\theta^I, \sin\theta^I]$. k_1 is the wavenumber evaluated using Mindlin plate theory and θ^I=arctan(y/x) is the incident wave propagation direction. The variable with superscript I indicates the wave parameter corresponding to the incident wave. In the case that the damage is a weak scattering inhomogeneity, $\left\|\hat{u}^S(\mathbf{x},\omega)\right\| \langle \langle \left\|\hat{u}^I(\mathbf{x},\omega)\right\|$, the scattered wave can be obtained using the Born approximation as (Wang and Chang 2005, Ng *et al*. 2012)

$$\hat{u}_B^S(\mathbf{x},\omega) = \iint\limits_\Omega \left[s_1 D\Gamma_{\beta\alpha}^I g_{3\alpha,\beta} + s_2\kappa^2 Gh\left(u_\alpha^I - \Omega_\alpha^I\right)\left(g_{3\alpha} + g_{33,\alpha}\right) + s_3\rho I\omega^2\Omega_\alpha^I g_{3\alpha} + s_4\rho h\omega^2 g_{33} \right]d^2\xi \tag{13}$$

where $\hat{u}_B^S$ is the scattered wave obtained by the Born approximation. The comma indicates the differentiation between subscripts $[\alpha,\beta]$=1,2. ξ represents an arbitrary point within the damage region. $\Gamma_{\alpha\beta}$ is the plate theory strain given by

$$\Gamma_{\alpha\beta} = \nu\Omega_{\alpha,\alpha}\delta_{\alpha\beta} + \frac{1-\nu}{2}\left(\Omega_{\alpha,\beta} + \Omega_{\beta,\alpha}\right) \tag{14}$$

where $\delta_{\alpha\beta}$ is the Kronecker delta. g_{31}, g_{32} and g_{33} are Green's functions (Rose and Wang 2004)

$$g_{31} = \gamma\frac{\partial H_0^{(1)}(k_1 r_s)}{\partial x}, \quad g_{32} = \gamma\frac{\partial H_0^{(1)}(k_1 r_s)}{\partial y}, \quad g_{33} = \gamma\frac{H_0^{(1)}(k_1 r_s)}{\lambda_1} \tag{15}$$

where $r_s = \sqrt{(x-\xi)^2 + (y-\eta)^2}$. $\gamma = i/4D(k_1^2 - k_2^2)$ and $\lambda_1 = 1 - \rho\omega^2/\kappa^2 Gk_1^2$. k_2 is the wavenumber of the second possible wave mode in Mindlin plate theory. $H_n^{(1)}(\cdot)$ represents the n-th order Hankel function of the first kind.

2.1.3 Reconstruction of perturbation functions by direct Fourier inversion

The Born approximation of the scattered wave in Eq. (13) can be simplified by considering the

far-field asymptotic expression of the Hankel function as (Wang and Chang 2005, Ng *et al.* 2012)

$$\lim_{\|\mathbf{k}\cdot\mathbf{x}\|\to\infty} H_0^{(1)}\left(k_1 r_s\right) \approx \sqrt{\frac{2}{\pi k_1 r_s}} e^{i\left(k_1 r_s - \frac{\pi}{4}\right)} \tag{16}$$

The scattered wave can then be expressed as (Wang and Rose 2003)

$$u_B^S\left(r_s, \theta^S, \theta^I, \omega\right) = \sum_{n=1}^{4}\left[P_n\left(k_1, \theta^S - \theta^I\right)\hat{S}_n\left(\mathbf{k}_1^S - \mathbf{k}_1^I\right)\sqrt{\frac{2}{\pi k_1 r_s}} e^{i\left(k_1 r_s - \frac{\pi}{4}\right)} \right] \tag{17}$$

where θ^I and θ^S are the angle of the incident and scattered waves, respectively. $\mathbf{k}_1^I = k_1[\cos\theta^I, \sin\theta^I]$ and $\mathbf{k}_1^S = k_1[\cos\theta^S, \sin\theta^S]$ are the incident and scattered wave vector. P_n for $n=1,2,3,4$ are defined as

$$P_1\left(k_1, \theta\right) = -\frac{i\gamma k_1^2}{4\left(k_1^2 + k_2^2\right)}\left(\cos^2\theta + \nu\sin^2\theta\right) \tag{18}$$

$$P_2\left(k_1, \theta\right) = -\frac{i\kappa^2 Gh k_1^2\left(1 - \gamma\right)^2}{4D\gamma\left(k_1^2 + k_2^2\right)}\cos\theta \tag{19}$$

$$P_3\left(k_1, \theta\right) = \frac{i\rho I\omega^2\gamma k_1^2}{4D\left(k_1^2 + k_2^2\right)}\cos\theta \tag{20}$$

$$P_4\left(k_1, \theta\right) = \frac{i\rho h\omega^2}{4D\gamma\left(k_1^2 + k_2^2\right)} \tag{21}$$

where $\hat{S}_n(\mathbf{k})$ is the two-dimensional (2D) Fourier transform of the perturbation functions, which are given as

$$\hat{S}_n\left(\mathbf{k}\right) = \iint_{\Sigma} s_n\left(\xi\right)e^{-i\mathbf{k}\cdot\xi}d\xi \tag{22}$$

Eq. (17) provides a linear relationship between the scattered wave and spatial transform values of $s_n(\xi)$ for $n=1,2,3,4$. However, the relative contribution of each of $s_n(\xi)$ depends on the type of damage. In the proposed method a combination of the perturbation functions $3s_1(\xi)=s_2(\xi)=3s_3(\xi)=s_4(\xi)$ is used for reconstructing the reduction in thickness due to corrosion in metallic plate structures. For a fixed incident wave angle θ^I, the measured scattered waves at various scattered angles θ^S provide values of Fourier transform $\hat{S}_n(\mathbf{k})$ on a circle in **k**-space with center $-\mathbf{k}_1^I$ and radius k_1 as shown in Fig. 3. Hence, the required data for image reconstruction, which is the data throughout a circular region of radius $2k_1$ in the **k**-space, can be obtained by varying the incident wave angle θ^I.

The perturbation functions $s_n(\xi)$, which provide a quantitative imaging of the damage, are evaluated by carrying out the 2D inverse Fourier transform of the obtained $\hat{S}_n(\mathbf{k})$ as
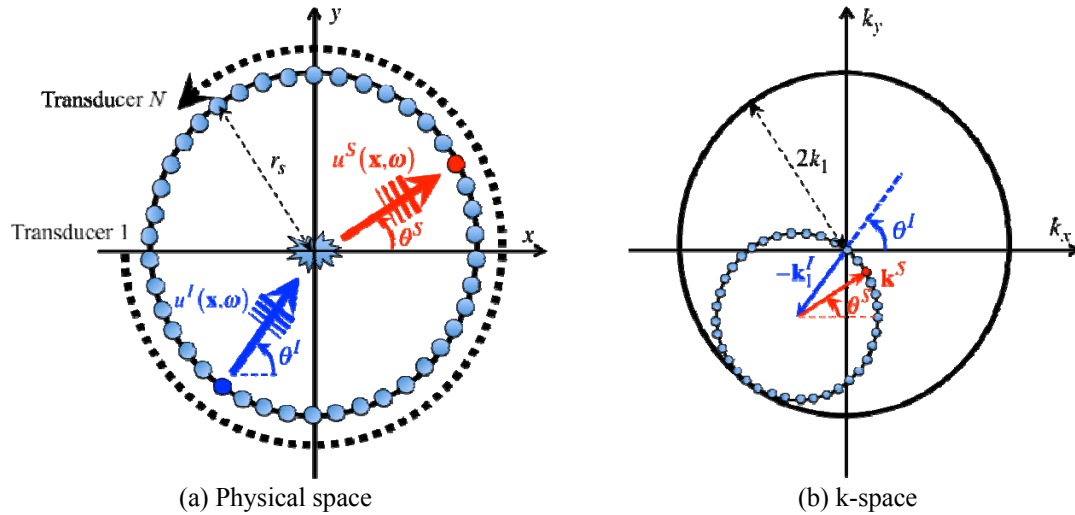
(a) Physical space   (b) k-space

Fig. 3 Schematic representation between physical space and **k-**space via Born approximation

where $\mathbf{k}=[k_x,k_y]=[k_1(\cos\theta^S-\cos\theta^I),k_1(\sin\theta^S-\sin\theta^I)]$. However, there is a computational difficulty for directing the Fourier inversion in the diffraction tomography. The scattered wave data must be cast onto a uniform calculation grid in **k**-space before the 2D inverse Fourier transform. The proposed method therefore employs a bilinear interpolation in the 2D Fourier interpolation.

As noted earlier, Lamb wave diffraction tomography assumes the weak scattering inhomogeneity must be located at the center of the transducer network. This limitation can be overcome by modifying the amplitude and phase of the measured scattered wave signals if the damage location is known. The proposed two-stage damage measurement technique overcomes this limitation by first determining the damage location during stage-one. The distance between the damage and the center of the transducer network is obtained in order to determine the required amplitude and phase modification for the scattered wave signals. The aforementioned Lamb wave diffraction tomography algorithm can then be employed to reconstruct the damage image using the modified scattered wave signals.

3. Numerical case studies

3.1 3D explicit finite element simulations

A 3D explicit FE method was used to simulate the Lamb wave propagation and scattering at damages in a steel plate. The dimension of the steel plate was $300\times300\times6$ mm^3. The material properties of the steel plate are summarized in Table 1. The numerical simulated data of a number

Table 1 Material properties of steel plate

E	v	ρ
203 GPa	0.29	7800 kg/m^3

Table 2 Location of transducer and corresponding scattering angles

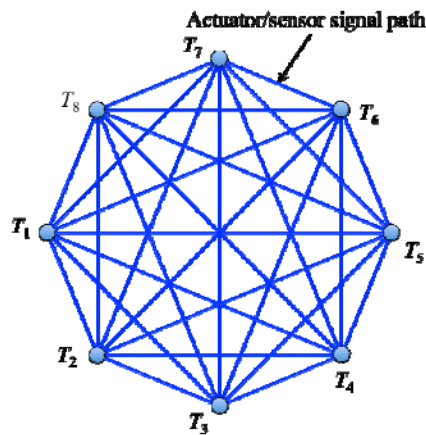| Transducer	x (mm)	y (mm)	Scattering angles (θ^S)
T_1	-50.00	0.00	180°
T_2	-35.36	-35.36	215°
T_3	0.00	-50.00	270°
T_4	35.36	-35.36	315°
T_5	50.00	0.00	0°
T_6	35.36	35.36	45°
T_7	0.00	50.00	90°
T_8	-35.36	35.36	135°

Fig. 4 Transducer network and signal paths

of case studies was then used to verify the proposed method. All numerical simulations in the current study were calculated using commercial FE software LS-DYNA, which employs the explicit central different integration scheme to calculate the response of the wave propagation. Eight-noded 3D reduced integration solid brick elements with hourglass control were used in the model, in which each node has three translation degrees of freedom.

It is assumed that eight circular piezoceramic transducers with 5 mm diameters were surface mounted to the plate to form a circular transducer network with a 100 mm diameter circular inspection region. These transducers were labeled in counter-clockwise order from T_1 to T_8 as shown in Fig. 4. As discussed in Section 2, the proposed method requires sequentially exciting the transducers from T_1 to T_8 to obtain the data for the proposed imaging algorithm. The signal paths in the sequential scan process are shown in Fig. 4. Table 2 summarizes the transducer locations and the corresponding scattering angles defined in Fig. 3(a).

The A_0 Lamb wave was excited by applying nodal displacement in the out-of-plane direction to surface FE nodes covered by the transducer to simulate a piston type excitation (Ng and Veidt 2012). A 200 kHz narrow band six-cycle sinusoidal tone burst pulse modulated by a Hanning window was used as the excitation signal. The wavelength of the A_0 Lamb wave at 200 kHz was 11.99 mm, which is in the same order of sizes as the damages of interest in this study. The out-of-plane displacement of the surface FE nodes located at the center of the transducers were calculated

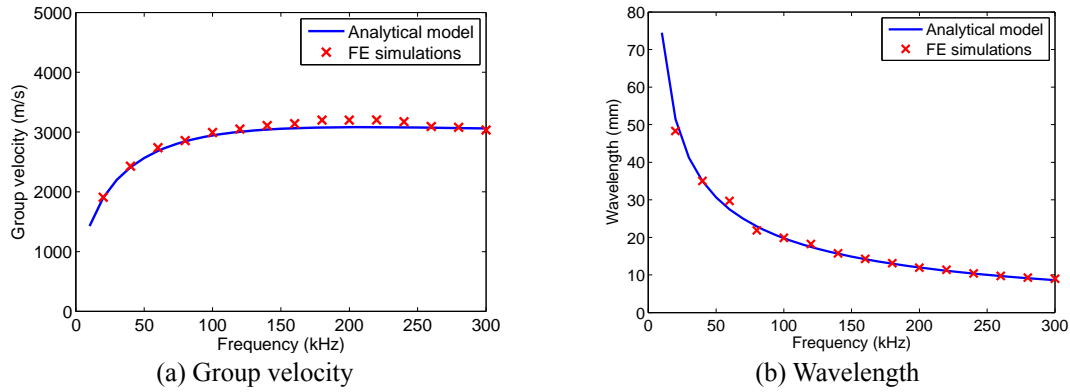(a) Group velocity   (b) Wavelength
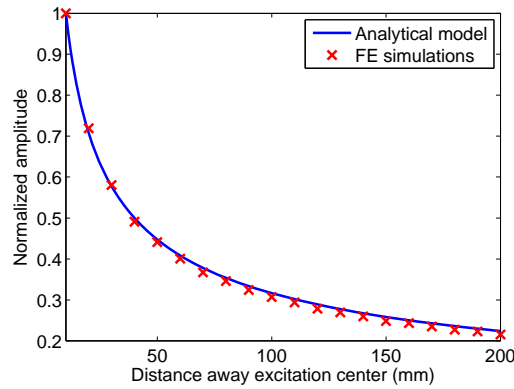
Fig. 5 Dispersion curves

Fig. 6 Normalized out-of-plane displacement amplitude as a function of wave propagation distance

and used in the proposed method. Most of the solid brick elements in the FE model had an in-plane square shape with dimensions 0.75×0.75 mm^2. The thickness of the solid brick elements was 0.375 mm, which ensured there were 16 layers of solid brick elements in the thickness direction of the plate. In the numerical simulation the maximum incremental time step, which ensures the stability of the dynamic analysis, was automatically controlled by LS-DYNA based on the element size and material properties. This means that there are at least 31 FE nodes per wavelength to ensure the accuracy of the simulation results. Hourglassing modes were minimized by applying suitable hourglass controls. The total hourglassing energy was less than 0.45% of the internal energy for all simulations.

Figs. 5(a) and 5(b) show the analytical results based on Mindlin plate theory and FE-calculated results of A_0 Lamb wave group velocity and wavelength dispersion curves. The dispersion curves of the FE simulation results were obtained by sweeping the excitation frequency from 20 kHz to 300 kHz in steps of 20 kHz. At each excitation frequency, Lamb wave signals were calculated at five locations. The group and phase velocity were calculated by averaging the results of all measurement points. In this study the group velocity was calculated using the energy density spectrum of the measured out-of-plane displacement by the Gabor wavelet transform as described in Section 2.1. The calculated phase velocity was then used to determine the wavelength of the excited A_0 Lamb wave.

Table 3 Summary of all damage cases in numerical case studies

Case	Defect location	Diameter	Percentage and type of thickness reduction
A	x=0.00 mm, y=0.00 mm	3.00 mm	12.5% symmetrical reduction of thickness
B	x=0.00 mm, y=0.00 mm	3.00 mm	6.25% non-symmetrical reduction of thickness
C	x=0.00 mm, y=0.00 mm	5.00 mm	6.25% non-symmetrical reduction of thickness
D	x=-15.00 mm, y=0.00 mm	3.00 mm	6.25% non-symmetrical reduction of thickness
E	x=-15.00 mm, y=15.00 mm	3.00 mm	6.25% non-symmetrical reduction of thickness

(a) Symmetrical reduction of thickness   (b) Non-symmetrical reduction of thickness
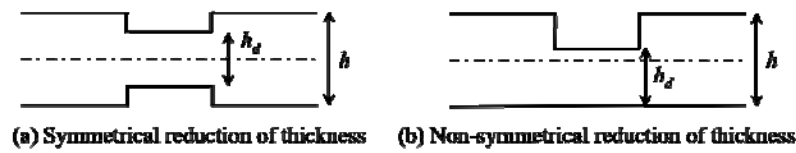
$$\text{Percentage of thickness reduction} = \frac{h - h_d}{h} \times 100\%$$

Fig. 7 Cross-section view of the plate thickness reduction

Fig. 6 shows the amplitude decay of the Lamb wave for a propagation distance between 10 mm to 200 mm with steps of 10 mm. In Fig. 6 the amplitudes of all measurement locations were normalized by the amplitude measured at 10 mm away from the excitation center. In Figs. 5 and 6 reasonable agreement was found between the analytical and FE simulation results. This observation demonstrated that the FE simulation could be used as a tool to validate the proposed defect imaging method. The small discrepancy between the analytical and FE simulation results in Figs. 5 and 6 can be treated as errors caused by measurement noise or modeling error in the numerical case studies simulating a practical situation.

Five cases of damage were considered in this study. They consisted of different sizes and types of thickness reductions to provide a comprehensive verification of the proposed damage imaging method. Defining the center of the transducer network as the origin, the details, such as damage location, diameter, and type and percentage of thickness reduction for each damage case, are summarized in Table 3.

3.2 Results of damage imaging

3.2.1 Case A: Symmetrical reduction of plate thickness located at the center of the transducer network

The damage considered in Case A was a 3 mm diameter circular plate thickness reduction located at x=0 mm, y=0 mm (center of the transducer network). The percentage of thickness reduction was 12.5% and was symmetrical about the mid-plane of the plate as shown in Fig. 7(a), and therefore, there was no mode conversion effect in the scattered waves. Case A was treated as a benchmark to demonstrate the proposed method. It should be noted that the imaging algorithms in stages-one and -two do not take into account the mode conversion effect in the image reconstruction. Case A, therefore, was considered the simplest damage condition and the condition most able to record the best performance in determining the damage location and plate thickness reduction.
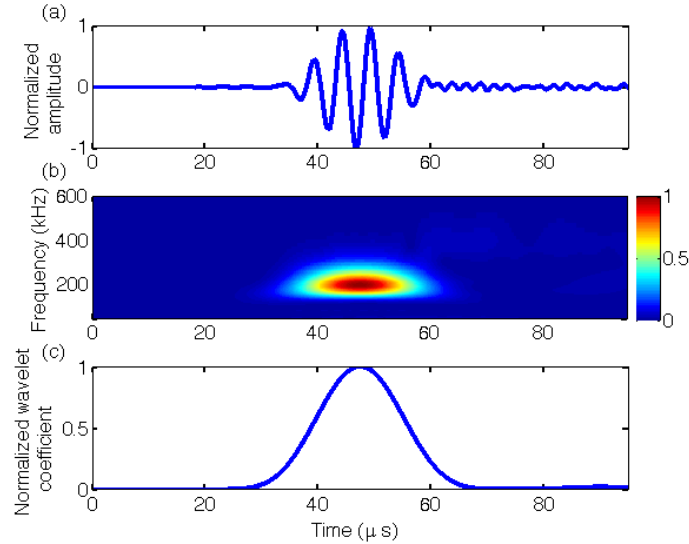
Fig. 8 (a) Scattered wave signal measured at transducer T_6 while T_1 is excited in Case A; (b) scaleogram obtained using Gabor wavelet transform; (c) normalized wavelet coefficient at excitation frequency 200 kHz

(a) Reconstructed damage location image (white cross: identified defect location; black circle: true defect location and size)

(b) Reconstructed plate thickness reduction percentage image (close up view at defect region; black circle: true defect location and size)

(c) Plate thickness reduction percentage profile across the damage (black solid line: reconstructed profile; blue dashed line: true profile)
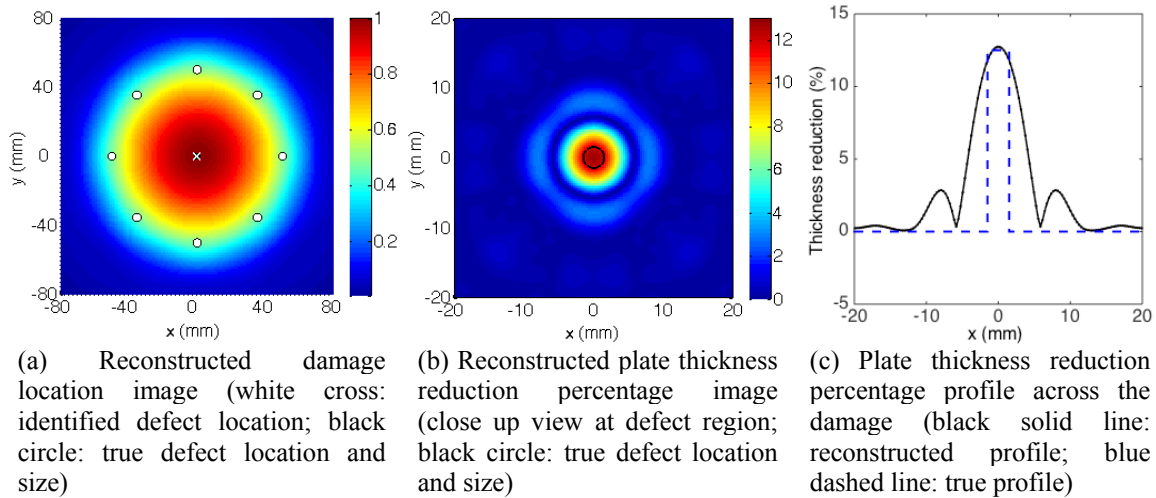
Fig. 9 Reconstructed image of the defect in Case A

As described in Section 2.1, the imaging algorithm in stage-one requires the scattered wave signals to be extracted using the baseline subtraction approach. Fig. 8(a) shows the scattered wave signal measured by transducer T_6 while T_1 was used for excitation. As shown in Fig. 8(b), the scaleogram of the scattered waves can be calculated using the Gabor wavelet transform as described in Section 2.1. The scaleogram indicates the energy distribution of the wave signal in the time-frequency domain. Fig. 8(c) shows the corresponding normalized wavelet coefficients at the excitation frequency, which were used as Eq. (4) to reconstruct an image for determining the damage location.

Table 4 Summary of identified damage locations

Case	Damage location	Identified location
A	x=0.00 mm, y=0.00 mm	x=0.00 mm, y=0.00 mm
B	x=0.00 mm, y=0.00 mm	x=0.00 mm, y=0.00 mm
C	x=0.00 mm, y=0.00 mm	x=0.00 mm, y=0.00 mm
D	x=-15.00 mm, y=0.00 mm	x=-14.00 mm, y=0.00 mm
E	x=-15.00 mm, y=15.00 mm	x=-16.00 mm, y=16.00 mm

(a) Reconstructed damage location image (white cross: identified defect location; black circle: true defect location and size)

(b) Reconstructed plate thickness reduction percentage image (close up view at defect region; black circle: true defect location and size)

(c) Plate thickness reduction percentage profile across the damage (black solid line: reconstructed profile; blue dashed line: true profile)
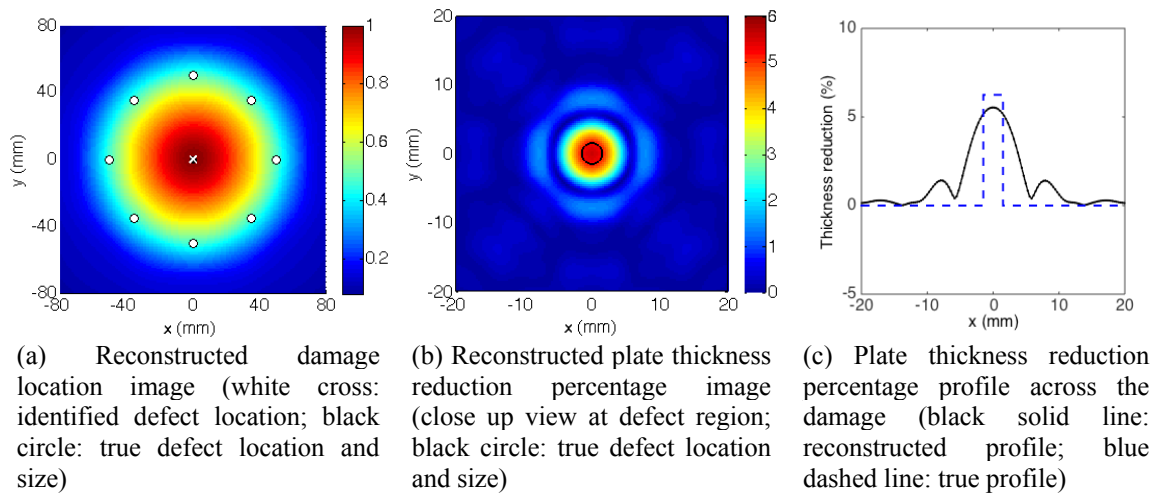
Fig. 10 Reconstructed image of the defect in Case B

Fig. 9(a) shows the reconstructed damage location image for Case A. The white circles indicate the transducer locations and the black circle is the true damage location and size. The damage location was determined by the image pixel having the maximum value. The identified damage location was marked with a white cross to accurately highlight the area of weakness. The identified damage location is also listed in Table 4. Fig. 9(b) shows a close up view of the central 40×40 mm^2 region of the plate thickness reduction percentage image reconstructed during stage-two of the proposed method. The corresponding plate thickness reduction percentage profile across the damage is shown in Fig. 9(c). The black solid and blue dashed lines are the reconstructed and true plate thickness reduction profile, respectively. There is a very good agreement between the reconstructed and true plate thickness reduction percentage in Case A.

3.2.2 Cases B and C: Non-symmetrical reduction of plate thickness located at the center of the transducer network

Cases B and C considered, respectively, a 3 mm and 5 mm diameter circular plate thickness reduction located at the center of the transducer network. The cases involved smaller percentages of thickness reduction (6.25% reduction of thickness) compared to Case A. The plate thickness reductions in Cases B and C were generated by reducing thickness at one side of the plate as shown in Fig. 7(b), and were therefore non-symmetrical about the mid-plane of the plate. The scattered waves in Cases B and C contain both fundamental symmetric mode (S_0) and A_0 Lamb waves. It should be noted that the proposed imaging method only takes into account the scattering
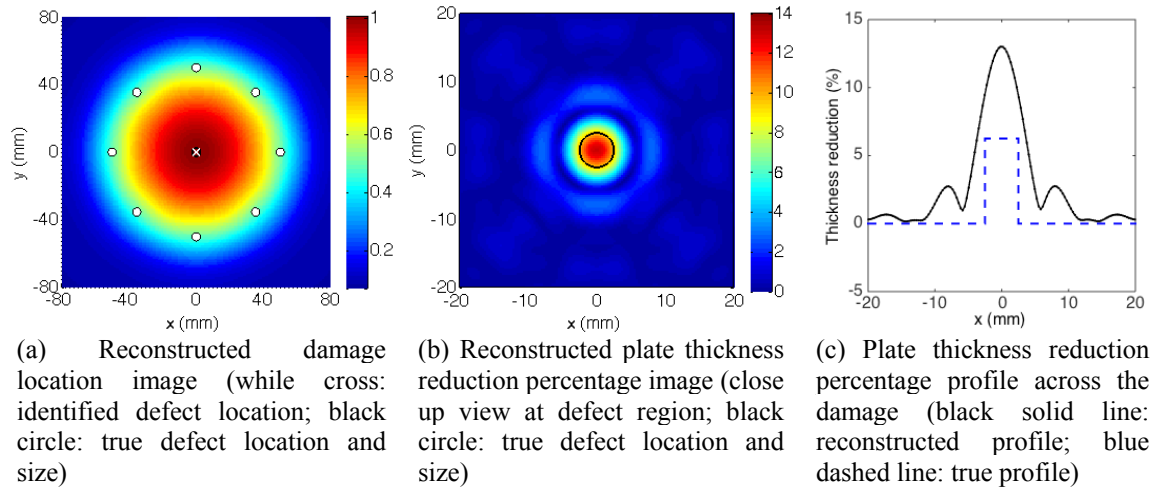
(a) Reconstructed damage location image (while cross: identified defect location; black circle: true defect location and size)

(b) Reconstructed plate thickness reduction percentage image (close up view at defect region; black circle: true defect location and size)

(c) Plate thickness reduction percentage profile across the damage (black solid line: reconstructed profile; blue dashed line: true profile)

Fig. 11 Reconstructed image of the defect in Case C

(a) Reconstructed damage location image (white cross: identified defect location; black circle: true defect location and size)

(b) Reconstructed plate thickness reduction percentage image (close up view at defect region; black circle: true defect location and size)
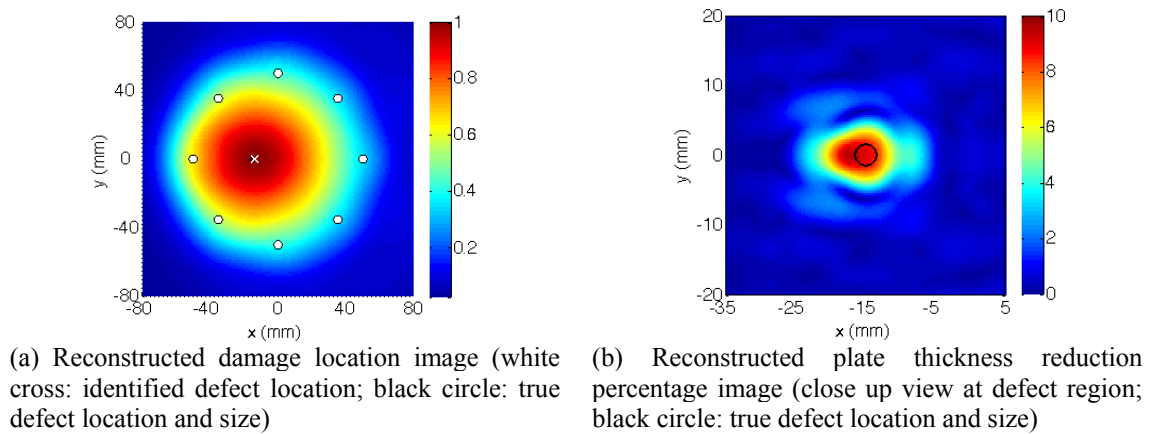
Fig. 12 Reconstructed images of the damage in Case D

of the A_0 Lamb wave. These two cases were therefore used to assess the performance of the proposed method in the presence of the mode conversion effect.

Figs. 10(a) and 11(a) show the reconstructed damage location for Cases B and C, respectively. Both images accurately indicate the damage location. The identified defect locations are listed in Table 4. Figs. 10(b) and 11(b) show the reconstructed plate thickness reduction percentage for Cases B and C, respectively. There is good agreement between the size indicated by the reconstructed plate thickness reduction percentage image and the true damage size. Figs. 10(c) and 11(c) show the plate thickness reduction percentage profile across the damage. Reasonable agreement was obtained between the reconstructed and true plate thickness reduction percentage profile in Case B. The results show that, although the imaging algorithms in stages-one and -two did not take into account the effect of mode conversion, the non-symmetrical reduction of plate thicknesses can still be reasonably identified from the reconstructed image.

However, the reconstructed and true plate thickness reduction percentage profile in Case C is greater than that in Case B as shown in Fig. 11(c). The reconstructed plate thickness reduction
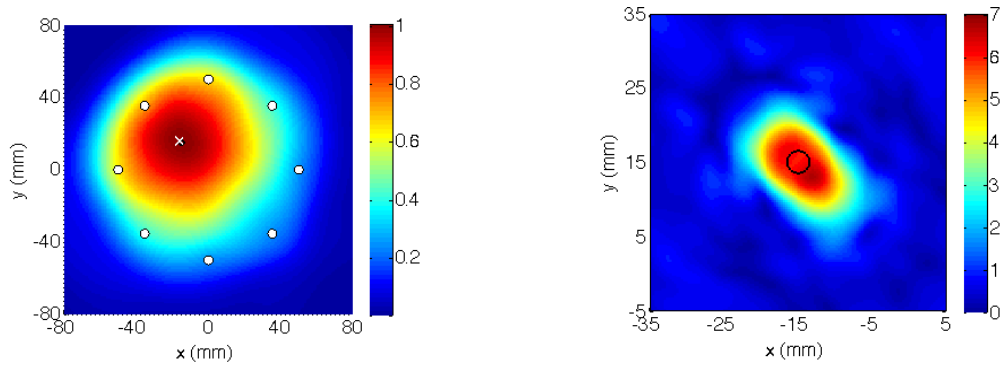
(a) Reconstructed plate location image (white cross: identified defect location; black circle: true defect location and size)

(b) Reconstructed plate thickness reduction percentage image (close up view at defect region; black circle: true defect location and size)

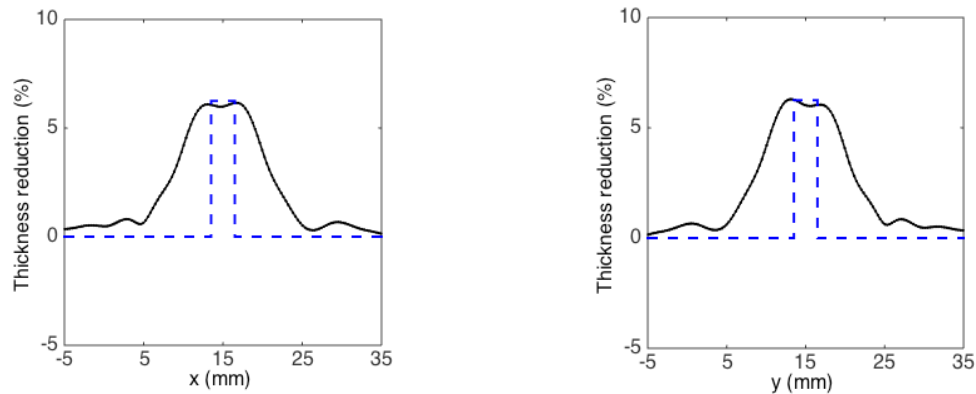Fig. 13 Plate thickness reduction percentage profile of the damage in Case E
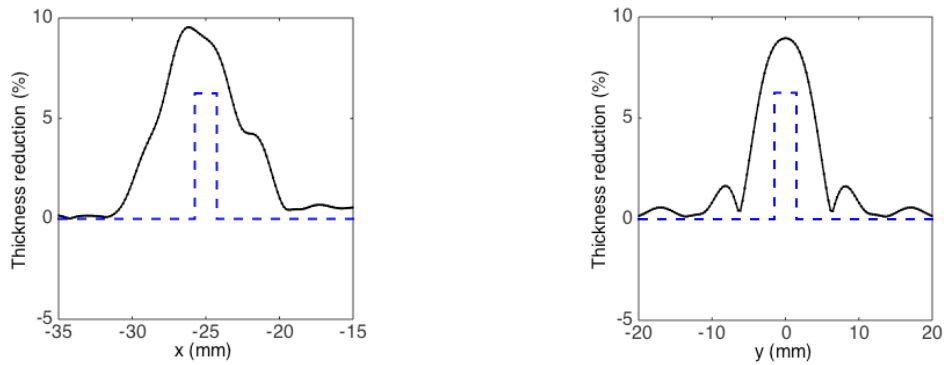
(a) Plate thickness reduction percentage profile across the damage in *x*-axis (black solid line: reconstructed profile; blue dashed line: true profile)

(b) Plate thickness reduction percentage profile across the damage in *y*-axis (black solid line: reconstructed profile; blue dashed line: true profile)

Fig. 14 Plate thickness reduction percentage profiles of the damage in Case D

percentage profile over-estimates the true thickness reduction, but the estimated and true values are still in the same order of magnitude. The main reason for this is that the diameter of the circular thickness reduction in Case C does not completely fulfill the weak scattering inhomogeneity assumption as discussed in Section 2.1.2, and the performance of the reconstructed plate thickness reduction percentage in Case C is not as good as that in Case B. It should be noted that the proposed method targets the early detection of damage. The weak scattering inhomogeneity is very suitable for this situation.

3.2.3 Cases D and E: Non-symmetrical reduction of plate thickness located off the center of the transducer network

Lamb wave diffraction tomography with far-field Born approximation assumes the damage is at the center of the transducer network. The proposed two-stage approach overcomes this limitation by first determining the location of the damage in stage-one, and then, modifying the

(a) Profile across the damage in *x*-axis (black solid line: reconstructed thickness reduction; blue dashed line: true thickness reduction)

(b) Profile across the damage in *y*-axis (black solid line: reconstructed thickness reduction; blue dashed line: true thickness reduction)

Fig. 15 Plate thickness reduction percentage profiles of the damage in Case E

amplitudes and phases of the scattering wave signals. The amplitude and phase modification allows the direct application of the far-field Born approximation in the damage imaging. However, the level of error in the identified damage location has an impact on the performance of the extended Lamb wave diffraction tomography in stage-two. Cases D and E considered plate thickness reduction with the same size and depth as Case B but they were located at *x*=-15 mm, *y*=0 mm and *x*=-15 mm, *y*=15 mm, respectively. The first objective of these two cases was to demonstrate the capacity of the proposed method to image damage located away from the center of the transducer network. The second objective was to evaluate the accuracy and the impact of the newly identified damage location error on the of the reconstructed plate thickness reduction image in stage-two of the proposed method.

   Fig. 12(a) and 13(a) are the reconstructed image of damage location images for Cases D and E. As indicated by the white crosses in both figures, the identified damage locations are *x*=-14 mm, *y*=0 mm and *x*=-16 mm, *y*=16 mm for Cases D and E, respectively. The identified damage locations are also listed in Table 4. The maximum damage location error is only 1 mm for a 100 mm diameter circular inspection area. The amplitude and phase of the scattered wave signals were then modified based on the identified damage locations. The modified scattered wave signals are the artificial equivalent of scattered waves from the damage, with the same size and shape but located at the center of the transducer network. Thus the Lamb wave diffraction tomography with the far-field Born approximation can be directly applied, using modified scattered wave signals to reconstruct a plate thickness reduction located away from the center of the transducer network. Figs. 12(b) and 13(b) show the reconstructed plate thickness reduction percentage images for Cases D and E, respectively. The corresponding thickness reduction percentage profiles across the damage on the *x*- and *y*- axes are shown in Figs. 14 and 15. Overall, the reconstructed thickness reduction percentage images of Cases D and E are not as accurate as Case B due to the error in the identified damage locations in stage-one. However, the reconstructed thickness reduction percentage images are still able to indicate reasonable size and depth of the plate thickness reduction.

4. Conclusions

This paper has proposed a two-stage approach for quantitative imaging of damages in metallic plates. The damages considered in this study were circular symmetrical and non-symmetrical reductions of plate thickness. In stage-one the location of the damage was determined by analyzing the cross-correlation of the wavelet coefficients extracted from incident pulses and scattered wave signals in the sequential scan process. The same set of scattered wave signals was then used to reconstruct the plate thickness reduction percentage image in stage-two for evaluating the damage. The method is practical in terms of the number of transducers required since only eight transducers are needed to achieve quantitative imaging of damage in plate structures.

The proposed two-stage imaging algorithm has been verified by a number of numerical case studies using 3D explicit FE simulations. This paper has demonstrated that the proposed two-stage approach is able to overcome the limitation of the Lamb wave diffraction tomography with far-field Born approximation. Hence the proposed methodology is applicable for damage at different locations within the transducer network. The results of the numerical case studies have shown that the proposed two-stage approach is able to accurately locate the damage with accuracy of the order of a few millimeters of a circular inspection area of $100mm^2$ and provide a reasonable estimation of the size and depth of the damage. Although the two-stage approach only takes into account the A_0 Lamb wave, the reconstructed image is still able to achieve reasonable accuracy for non-symmetrical reduction of plate thickness, in which the mode conversion occurs in the Lamb wave scattering. Further research work is to carry out experimental studies for demonstrating the practicability of the proposed method in real applications.

Acknowledgments

References

Achenbach, J.D. (2000), "Quantitative nondestructive evaluation", *Int J. Solids Struct.*, **37**, 13-27.
Alleyne, D., Pavlakovic, B., Lowe, M. and Cawley, P. (2001), "Rapid, long range inspection of chemical plant pipework using guided waves", *Insight*, **43**(2), 93-96.
Belanger, P. and Cawley, P. (2009), "Feasibility of low frequency straight-ray guided wave tomography", *NDT and E Int.*, **42**(2), 113-119.
Belanger, P., Cawley, P. and Simonetti, F. (2010), "Guided wave diffraction tomography within the Born approximation", *IEEE Trans. Ultra. Ferr. Freq. Cont.*, **57**(6), 1405-1418.
Carden, E.P. and Fanning, P. (2004), "Vibration based condition monitoring: a review", *Struct. Hlth. Monit.*, **3**, 355-377.
Chan, E., Wang, C.H. and Rose, F.L.R. (2014), "Characterization of laminar damage in an aluminum panel by diffraction tomogxraphy based imaging method using Lamb waves", *7th European Workshop on Structural Health Monitoring*, Nantes, France.
Farrar, C.R. and Worden, K. (2007), "An introduction to structural health monitoring", *Phil. Trans. R. Soc. A.*, **365**, 303-315.

Graff, K.F. (1991), *Wave Motion in Elastic Solids*, Dover Publications Inc., New York, United States.

Huthwaite, P. and Simonetti, F. (2013), "High-resolution guided wave tomography", *Wave Motion*, **50**(5), 979-993.

Jansen, D.P. and Hutchins, D.A. (1990), "Lamb wave tomography", *IEEE Ultrasonics Symposium Proceedings*, Honolulu, HI, December, 1017-1020.

Kishimoto, K., Inoue, H., Hamada, M. and Shibuya, T. (1995), "Time frequency analysis of dispersive waves by means of wavelet transform", *J. Appl. Mech.*, **62**, 841-848.

Lam, H.F., Ng, C.T. and Leung, A.Y.T. (2008), "Multicrack detection on semirigidly connected beams utilizing dynamic data", *J. Eng. Mech.*, ASCE, **134**(1), 90-99.

Leonard, K.R. and Hinder, M.K. (2005), "Lamb wave tomography of pipe-like structures", *Ultrasonics*, **43**, 574-583.

Leonard, K.R., Malyarenko, E.V. and Hinders, M.K. (2002), "Ultrasonic Lamb wave tomography", *Inver. Probl.*, **18**(6), 1795-1808.

Lin, X. and Yuan, F.G. (2001), "Damage detection of a plate using migration technique", *J. Intel. Mater. Syst. Struct.*, **12**(7), 469-482.

Malyarenko, E.V. and Hinders, M.K. (2000), "Fan beam and double crosshole Lamb wave tomography for mapping flows in aging aircraft structures", *J. Acoust. Soc. Am.*, **108**(4), 1631-1639.

Malyarenko, E.V. and Hinders, M.K. (2001), "Ultrasonic Lamb wave diffraction tomography", *Ultrasonics*, **39**(4), 269-281.

Ng, C.T. (2014), "Bayesian model updating approach for experimental identification of damage ion beams using guided waves", *Struct. Hlth. Monit.*, **13**, 359-373.

Ng, C.T. (2014), "On the selection of advanced signal processing techniques for guided wave damage identification using a statistical approach", *Eng. Struct.*, **67**, 50-60.

Ng, C.T. and Veidt, M. (2009), "A Lamb-wave-based technique for damage detection in composite laminates", *Smart Mater. Struct.*, **18**(7), 1-12.

Ng, C.T. and Veidt, M. (2012), "Scattering characteristics of Lamb waves from debondings at structural features in composite laminates", *J. Acoust. Soc. Am.*, **132**(1), 115-123.

Ng, C.T., Veidt, M. and Lam, H.F. (2009a), "Guided wave damage characterization in beams utilizing probabilistic optimization", *Eng. Struct.*, **31**(12), 2842-2850.

Ng, C.T., Veidt, M. and Rajic, N. (2009b), "Integrated piezoceramic transducers for imaging damage in composite laminates", *Proceedings of SPIE*, 7493M, 1-8.

Ng, C.T., Veidt, M. Rose, L.R.F. and Wang, C.H. (2012), "Analytical and finite element prediction of Lamb wave scattering at delaminations in quasi-isotropic composite laminates", *J. Sound Vib.*, **331**(22), 4870-4883.

Rohde, A.H., Rose, L.R.F., Veidt, M. and Homer, J. (2008), "A computer simulation study of imaging flexural inhomogeneities using plate wave diffraction tomography", *Ultrasonics*, **48**, 6-15.

Rohde, A.H., Rose, L.R.F., Veidt, M. and Wang, C.H. (2009), "Two inversion strategies for plate wave diffraction tomography", *Mater. Forum*, **33**, 489-495.

Rose, J.L. (2002), "A baseline and vision of ultrasonic guided wave inspection potential", *J. Press. Ves. Tech.*, **124**, 273-282.

Rose, L.R. and Wang, C.H. (2010), "Mindlin plate theory for damage detection: imaging of flexural inhomogeneities", *J. Acoust. Soc. Am.*, **127**(2), 754-763.

Rose, L.R.F. and Wang, C.H. (2004), "Mindlin plate theory for damage detection: source solutions", *J. Acoust. Soc. Am.*, **116**, 154-171.

Veidt, M, Ng, C.T., Hames, S. and Wattinger, T. (2008), "Imaging laminar damage in plates using Lamb wave beamforming", *Adv. Mater. Res.*, **47**(50), 666-669.

Veidt, M. and Ng, C.T. (2011), "Influence of stacking sequence on scattering characteristics of the fundamental anti-symmetric Lamb wave at through holes in composite laminates", *J. Acoust. Soc. Am.*, **129**(3), 1280-1287.

Virrmani, Y.P. (2002), *Corrosion Costs and Preventive Strategies in the United States*, Technical Brief, FHWA-RD-01-156, Federal Highway Administration, U.S. Department of Transportation, Washington,

DC.

Wang, C.H. and Chang, F.K. (2005), "Scattering of plate waves by a cylindrical inhomogeneity", *J. Sound Vib.*, **282**, 429-451.

Wang, C.H. and Rose, L.R.F. (2003), "Plate-wave diffraction tomography for structural health monitoring", *Rev. Quant. Nondestr. Eval.*, **22**, 1615-1622.

Wang, C.H. and Rose, L.R.F. (2013), "Minimum sensor density for quantitative damage imaging", *9th Int. Workshop on Struct. health Monitoring*, Stanford, USA.

Wang, C.H., Rose, J.T. and Chang, F.K. (2004), "A synthetic time-reversal imaging method for structural health monitoring", *Smart Mater. Struct.*, **13**, 415-423.

CN